

Initiation and Organizational Modes of an Extreme-Rain-Producing Mesoscale Convective System along a Mei-Yu Front in East China

YALI LUO

State Key Laboratory of Severe Weather, Chinese Academy of Meteorological Sciences, Beijing, China

YU GONG

National Meteorological Center, Chinese Meteorological Administration, Beijing, China

DA-LIN ZHANG

*State Key Laboratory of Severe Weather, Chinese Academy of Meteorological Sciences, Beijing, China,
and Department of Atmospheric and Oceanic Science, University of Maryland, College Park, College Park, Maryland*

(Manuscript received 6 April 2013, in final form 24 August 2013)

ABSTRACT

The initiation and organization of a quasi-linear extreme-rain-producing mesoscale convective system (MCS) along a mei-yu front in east China during the midnight-to-morning hours of 8 July 2007 are studied using high-resolution surface observations and radar reflectivity, and a 24-h convection-permitting simulation with the nested grid spacing of 1.11 km. Both the observations and the simulation reveal that the quasi-linear MCS forms through continuous convective initiation and organization into west–east-oriented rainbands with life spans of about 4–10 h, and their subsequent southeastward propagation. Results show that the early convective initiation at the western end of the MCS results from moist southwesterly monsoonal flows ascending cold domes left behind by convective activity that develops during the previous afternoon-to-evening hours, suggesting a possible linkage between the early morning and late afternoon peaks of the mei-yu rainfall. Two scales of convective organization are found during the MCS's development: one is the east- to northeastward “echo training” of convective cells along individual rainbands, and the other is the southeastward “band training” of the rainbands along the quasi-linear MCS. The two organizational modes are similar within the context of “training” of convective elements, but they differ in their spatial scales and movement directions. It is concluded that the repeated convective backbuilding and the subsequent echo training along the same path account for the extreme rainfall production in the present case, whereas the band training is responsible for the longevity of the rainbands and the formation of the quasi-linear MCS.

1. Introduction

The mei-yu season over the Yangtze–Huai Rivers basin (YHRB; see Fig. 1 for the distribution of the two rivers), typically occurring during the period from mid-June to mid-July, is one of the three heavy-rainfall periods over China (e.g., Ding 1992). Numerous observational and modeling studies have been conducted in the past three decades to examine the large-scale circulation, synoptic-scale weather systems, mesoscale convective systems

(MCSs), and cloud-precipitation morphology associated with the mei-yu rainfall (Chen and Yu 1988; Chen et al. 1998; Qian et al. 2004; Ding and Chan 2005). Most of the previous studies have attributed the generation of heavy rainfall to the continuous lifting of moist monsoonal air at the mei-yu front that is characterized by weak temperature gradients but high equivalent potential temperature θ_e gradients (Ding and Chan 2005). Because of its quasi-stationary character, the YHRB experiences heavy rainfall often as a series of convective cells moves over the same region along the mei-yu front—the so-called echo-training process (Doswell et al. 1996).

Only recently has the rapid growth of computing power allowed real-data convection-permitting studies of MCSs with a grid spacing of 1–4 km (Lean et al. 2008;

Corresponding author address: Dr. Yali Luo, State Key Laboratory of Severe Weather, Chinese Academy of Meteorological Sciences, Beijing 100081, China.
E-mail: yali@cams.cma.gov.cn

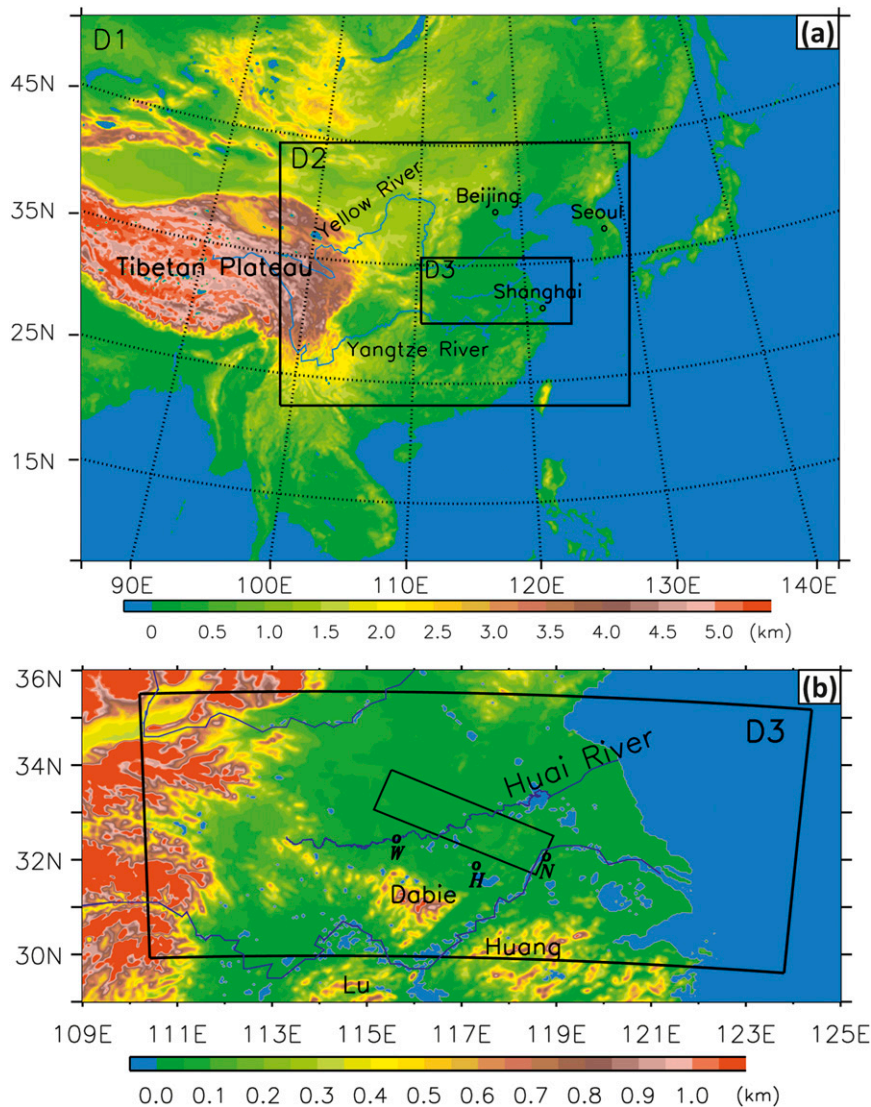


FIG. 1. (a) Topography (shadings) in the simulation domains (D1, D2, and D3). The Tibetan Plateau and the Yangtze and Yellow Rivers (blue lines), along with a few cities, are labeled. (b) Topography (shadings) over the inner-most domain (D3). The rectangular box denotes the control region used in the present study. The Huai River (blue line), and Mounts Dabie, Huang, and Lu are labeled. The small black circles above the letters W, H, and N represent the Wangjiaba reservoir and the cities of Hefei and Nanjing, respectively. The remaining figures also adopt this labeling convention.

Kain et al. 2008; Schwartz et al. 2009). Of relevance to the present study is a cloud-resolving simulation of a heavy-rain-producing MCS that occurred during the mei-yu season of July 2003 with the nested grid size of 444 m by Zhang and Zhang (2012, hereafter ZZ12). ZZ12 demonstrate the important roles of isentropic lifting of moist monsoonal air over convectively generated cold domes in triggering deep convection, of a low-level jet (LLJ) in maintaining conditional instability, and of the echo training in producing the heavy rainfall.

Recently, the mei-yu rainfall over YHRB was found to exhibit two diurnal peaks: one in the early morning with a duration of more than 6 h and the other in the late afternoon of 1–3-h duration (Yu et al. 2007; Zhou et al. 2008; Yuan et al. 2010; Yuan et al. 2012; Luo et al. 2013). Mechanisms that govern the formation of the early morning rainfall peak are not well known, despite numerous studies on the mei-yu rainfall over YHRB. Although the importance of the low-level southwesterly flow has been noticed (Chen et al. 2010), our knowledge

about the important processes at the meso- and smaller scales is lacking. In particular, details of the initiation and organization of MCSs are essentially unavailable in the literature due to the lack of high-resolution observations. Convective initiation, surface mesoscale features, and echo-training phenomena shown in ZZ12 are based on a cloud-resolving simulation with few observational supports.

The present study focuses on an extreme rainfall event that occurred over YHRB during the midnight-to-morning hours [i.e., 0000–1400 Beijing standard time (BST), BST = UTC + 8 h] of 8 July 2007. The mei-yu season of 2007 was well known in China for having the worst flood in the Huai River valley since 1954 due to the development of several heavy rainfall events and the unusually long rainy period over the region from 19 June to 26 July (Zhao et al. 2007). The extreme rainfall event under study was the heaviest one during the season. Figure 2a shows the 14-h accumulated rainfall distribution exhibiting an elongated rainfall belt of more than 700 km in length and 100–200 km in width, with the peak amount of 298 mm; it was nearly west–east (northwest–southeast) oriented to the west (east) of the Huai River. In this study, we focus more on the western portion of this rainfall belt, as highlighted by a rectangular box of about 360 km \times 100 km in Fig. 2a, where a majority of rain gauge stations receiving more than 200 mm of rainfall are located. Thus, the elongated rectangular box is hereafter referred to as the control region or box. Because of the persistent heavy rainfall, the water level of Wangjiaba’s reservoir, as denoted by the “W” in Fig. 2, was up to 29.4 m on 9 July. It exceeded the reservoir warning level by 1.8 m and prompted the Chinese Ministry of Water Resources to make a sluice in the reservoir.

The major objectives of the present study are twofold: (i) to investigate the mechanisms governing the nocturnal convective initiation along the mei-yu front and (ii) to document the meso- γ - to meso- β -scale organizations of the associated MCS that developed during the midnight-to-early morning period and weakened in the afternoon hours of 8 July 2007. The objectives will be achieved through multiscale observational analyses and a 24-h numerical simulation of the MCS with the nested 1.1-km grid spacing. The observational data used herein include the mosaic radar reflectivity data and the 8-km resolution rainfall, whose high quality has been shown by Luo et al. (2013), surface observations of air temperature, wind direction and speed, and pressure at automatic weather stations that were carefully quality controlled.

It should be mentioned that Luo et al. (2010) have studied this extreme rainfall event, but they focused

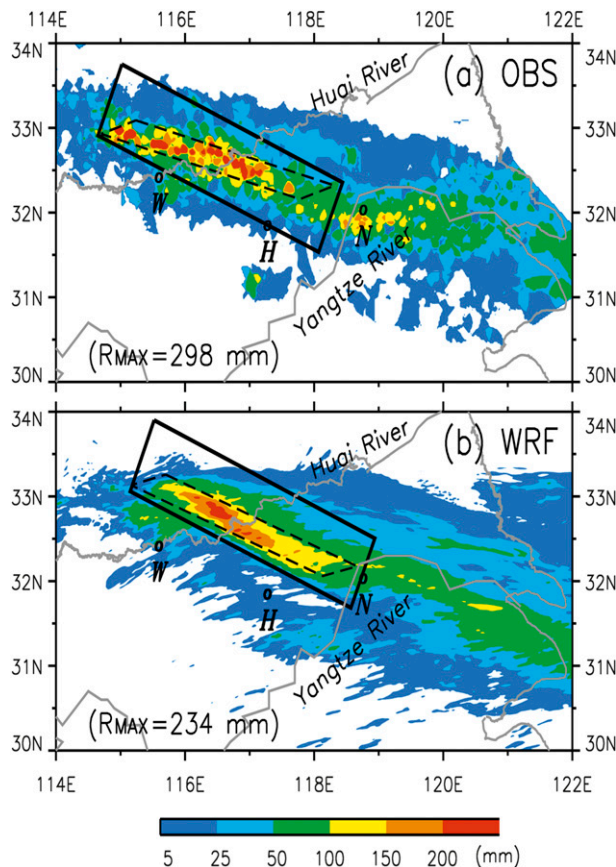


FIG. 2. Distribution of the 14-h accumulated surface rainfall (shaded, mm) during the period of 0000–1400 BST 8 Jul 2007 derived from (a) the 8-km resolution gridded hourly rainfall analysis and (b) the model simulation from the finest-resolution (1.1 km) domain. The rectangular box in black denotes the control region. Note that slightly different locations of the control region in (a) and (b) are given due to some position errors in the simulated MCS (see text). The narrow elongated zones (dashed) in (a) and (b) are used to plot the Hovmöller diagrams in Figs. 11a and 11b, respectively. The Yangtze and Huai Rivers and coastlines are plotted in gray. The black circles above the letters W, H, and N represent the Wangjiaba reservoir and the cities of Hefei and Nanjing, respectively. RMAX denotes the maximum accumulated rainfall amount (mm).

mostly on its associated microphysical processes and their coupling with dynamical processes leading to the generation of convective and stratiform rainfall. Their results were obtained using eight convection-permitting simulations with different cloud microphysics schemes and the nested-grid size of 3.33 km. The above-mentioned objectives were not pursued.

The next section shows a sequence of radar reflectivity from the mosaic reflectivity data during the life cycle of the MCS, and provides an overview of the large-scale conditions under which the torrential rainfall was generated. Section 3 provides a brief description of the Weather Research and Forecasting Model (WRF) and

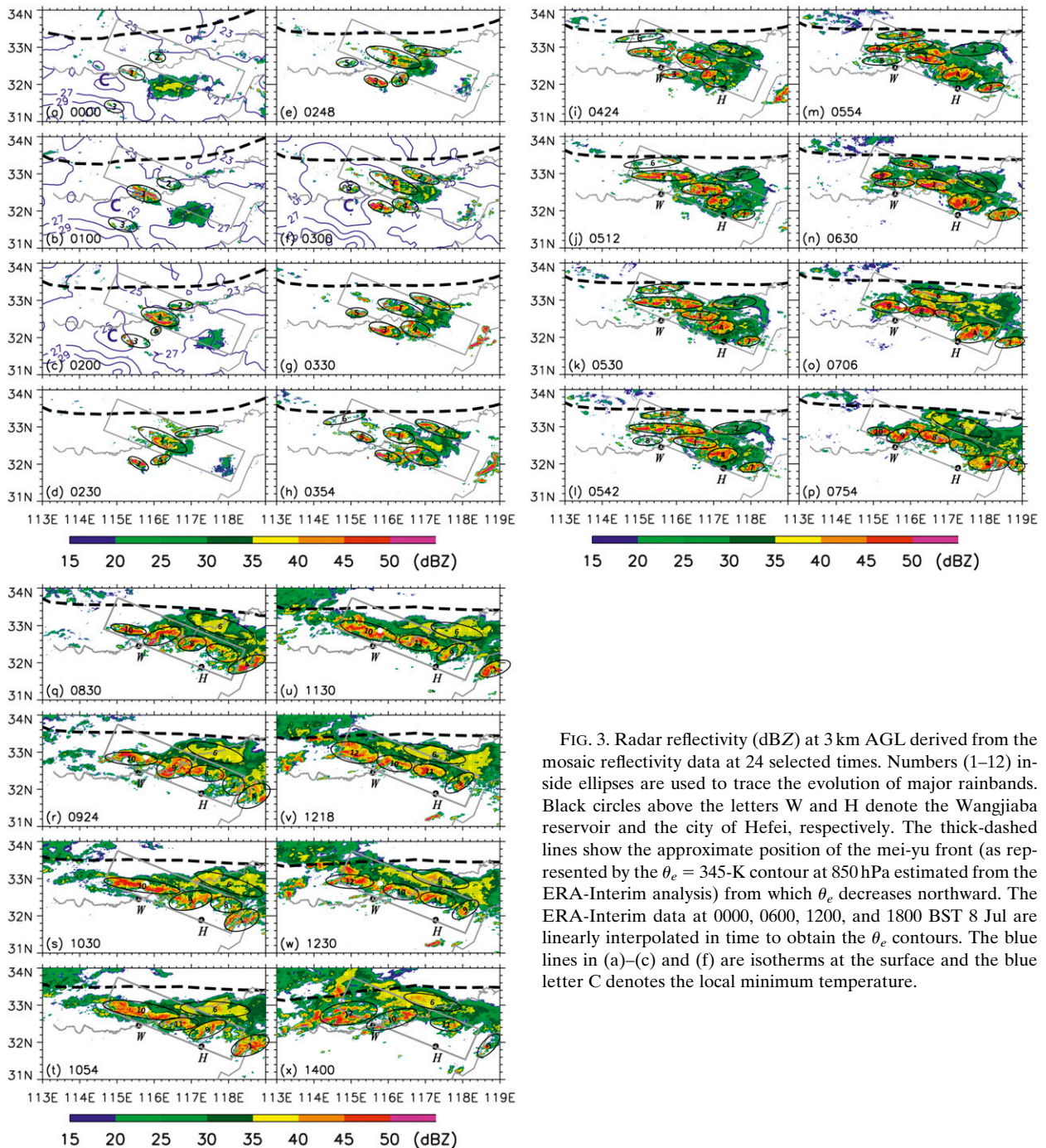


FIG. 3. Radar reflectivity (dBZ) at 3 km AGL derived from the mosaic reflectivity data at 24 selected times. Numbers (1–12) inside ellipses are used to trace the evolution of major rainbands. Black circles above the letters W and H denote the Wangjiaba reservoir and the city of Hefei, respectively. The thick-dashed lines show the approximate position of the mei-yu front (as represented by the $\theta_e = 345\text{-K}$ contour at 850 hPa estimated from the ERA-Interim analysis) from which θ_e decreases northward. The ERA-Interim data at 0000, 0600, 1200, and 1800 BST 8 Jul are linearly interpolated in time to obtain the θ_e contours. The blue lines in (a)–(c) and (f) are isotherms at the surface and the blue letter C denotes the local minimum temperature.

shows verifications of the 24-h simulation against all available high-resolution observations. Section 4 examines the initiation of the 8 July 2007 MCS. Section 5 presents the three-dimensional structures associated with the extreme-rain-producing MCS, especially the echo-raining process and the propagation of convective rainbands along the same path leading to the extreme rainfall. A summary and conclusions, including a conceptual

model of the MCS and its associated extreme rainfall production, are presented in the final section.

2. Observational analysis

To help understand the generation of the quasi-linear torrential rainfall belt given in Fig. 2a, we present first in Fig. 3 the time sequence of radar reflectivity at 3 km

above ground level (AGL) during the life cycle of the MCS. One can see many finescale structural features and the detailed evolution of the extreme-rain-producing MCS due to the use of the newly available high-resolution ($0.01^\circ \times 0.01^\circ$) mosaic radar reflectivity data (Luo et al. 2013). This MCS was initiated near midnight (i.e., 0000 BST 8 July) and then organized in a quasi-linear fashion consisting of numerous well-defined, near-west–east-oriented band-shaped convective precipitation regions of reflectivity >35 dBZ (simply referred to herein as rainbands) during its life span. Specifically, we have traced major rainbands of interest in Fig. 3 from the 6-min resolution reflectivity data, and labeled them sequentially based on the time of their first appearances. It is difficult to quantitatively define the beginning and ending of a rainband because of the splitting of a rainband and merging of different rainbands.

Figure 3a shows two banded precipitation areas at the initiating time: one close to Wangjiaba (W) with strong echoes but small coverage (labeled as 1), and the other between W and H with weak echoes but larger coverage (referred to as WH). The latter propagated eastward to the eastern edge of the control region and diminished in 3 h (Fig. 3d), contributing little to the total rainfall in the control box. However, WH developed in the previous afternoon-to-evening hours and left behind a meso- β -scale cold dome (Figs. 3a–c and 3f) that appeared to play an important role in triggering the nocturnal convection during the early development stage of the MCS of interest (section 4).

Rainband 1 grew in length as it moved northeastward into the control region (Fig. 3b). By 0330 BST, it moved close to the central axis of the elongated control box with stratiform rainfall to the east (Fig. 3g). During the period of 0000–0530 BST (Figs. 3a–k), we see the initiation and organization of rainband 2 to the north of rainband 1, rainbands 3 and 4 to the south of rainband 1, and rainbands 5 and 6 to the west. As the old rainbands propagated eastward, rainband 2 became stratiform due to its downstream location with respect to the source of the energy supply, while the backbuilding of convective cells allowed rainband 5 to extend from the southwest corner of the control box to the Huai River with a length scale of over 200 km. Rainband 3 dissipated shortly after it moved into the control box at about 0512 BST, when rainband 7 initiated over the southeastern corner of the control box due likely to the lifting of outflows from rainband 4.

At 0530 BST, we see six well-defined rainbands that were either west–east or southwest–northeast oriented, depending on their distribution on the west or east side of the Huai River (Fig. 3k). About 10 min later, new echoes of about 30 dBZ appeared over the southwestern

corner of the control box that formed rainband 8 at about 0630 BST. By 0554 BST, rainband 5 split into two segments (the western one is labeled rainband 9), due likely to the different propagation speeds between the southeastward-moving rainband and the eastward-moving convective cells in the backbuilding region. These rainbands were observed to move southeastward along the same area, while convective cells, after their formation, tended to move eastward along individual rainbands; they are referred to herein as band training and echo training, respectively, rather than simply echo training, as in Doswell et al. (1996). The life spans of these rainbands varied roughly from 4 h (e.g., rainbands 2 and 3) to about 10 h (e.g., rainband 1).

Most of the extreme rainfall was generated during the 5-h period of 0700–1200 BST 8 July when the backbuilding pattern of radar reflectivity remained quasi-stationary and highly organized in linear fashion, that is, west–east oriented to the west of and northeast–southwest oriented to the east of the Huai River (cf. Figs. 3o–u and 2a). The backbuilding and echo-band training processes could account for the generation of the extreme rainfall in the present case (cf. Figs. 2a and 3), which are to a certain extent similar to the backbuilding conceptual model of extreme-rain-producing MCSs by Schumacher and Johnson (2005) except for the organized rainband structures and evolution. The echo-training process appeared to dominate for the west–east-oriented portion of the rainfall belt shown in Fig. 2a. Shortly after 1200 BST, the quasi-linear MCS began to break into scattered convective clusters consisting of numerous southwest–northeast-oriented short rainbands, despite the continued backbuilding to the southwest of the control region (Figs. 3w and 3x). Thus, the quasi-linear MCS over the control box dissipated quickly during the early afternoon hours of 8 July.

One may note the distribution of a long but weak precipitation region between the quasi-linear MCS and the mei-yu front (the $\theta_e = 345$ -K contours in Fig. 3) after 0706 BST (Figs. 3o–x). This precipitation region could be clearly traced back to the dissipation of rainband 6 as it moved to the rear of the quasi-linear MCS (cf. Figs. 3h–j). Like rainband 2, its eastern portion evolved into stratiform rain at later stages (Fig. 3h) as a result of the reduced energy supply. Thus, the origin of this weak (stratiform) precipitation region differs from the trailing stratiform region in the conceptual model of a mid-latitude mature squall line by Houze et al. (1989) and that in a model-simulated one (Zhang et al. 1989). However, the detrainment of buoyant air and hydrometeors from the quasi-linear MCS could contribute to the maintenance of the stratiform precipitation (Luo et al. 2010), which is similar in some sense to that

described by Houze et al. (1989). The backbuilding and echo-training processes appeared to account for the westward extension of the weak precipitation region during the weakening stage (Figs. 3v–x). Nevertheless, this rainband contributed little to the total rainfall production (cf. Figs. 3o–x and 2a).

Figure 4 shows the major features of the large-scale conditions during the extreme rainfall event. During the extreme rainfall period, the lower half of the troposphere over south China was dominated by an anticyclonic circulation associated with a subtropical high centered over the western Pacific, with a moist southerly monsoonal flow of $10\text{--}15\text{ m s}^{-1}$ immediately to the east of the Tibetan Plateau, but weak and much drier airflows over southeast China. If the mei-yu front is defined as roughly corresponding to the $\theta_e = 345\text{-K}$ surface (Fig. 4b), following ZZ12, the torrential rainfall event occurred just at the southern side of the mei-yu front, where sharp θ_e gradients and pronounced horizontal wind shear were present. Of relevance is that the northwest–southeast-oriented control region was situated in a narrow zone of the westerly current of high- θ_e air (Fig. 4b) with the precipitable water exceeding 60 mm (Fig. 4c). The lower- θ_e air and a cold mesolow pressure system to the north of the control region seem to play a role in maintaining the quasi-stationary mei-yu front. Little thermal advection occurred upstream in the lower half of the troposphere (Fig. 4c), except at 500 hPa where there was weak warm advection upstream (e.g., Fig. 4a), unlike another YHRB torrential-rainfall event (4 July 2003) studied by ZZ12, in which some cold advection behind a 700-hPa trough played a role. Moreover, the frontal-scale ascent in the vicinity of the mei-yu front is very weak ($<0.01\text{ m s}^{-1}$; not shown) during the MCS's life span.

In summary, the tropical high- θ_e air could not be lifted during its northeastward and then eastward course under the influence of the subtropical high until it arrived at the control region ahead of the mei-yu front. The presence of the high precipitable water provided a favorable moist environment for heavy rainfall production. However, the above analysis could not reveal beforehand the exact location of the convective initiation, the distribution, evolution, and intensity of the rainfall, even after considering the roles of the mei-yu front. Furthermore, what conditions favor the initiation of the linear MCS over the western control box? Why were there two scales of convective organizations (i.e., echo and band training)? How did they contribute to the generation of the torrential rainfall? For all of these questions and issues, we have to invoke the use of a convection-permitting simulation to examine the mesoscale processes leading to the development of the present extreme rainfall event.

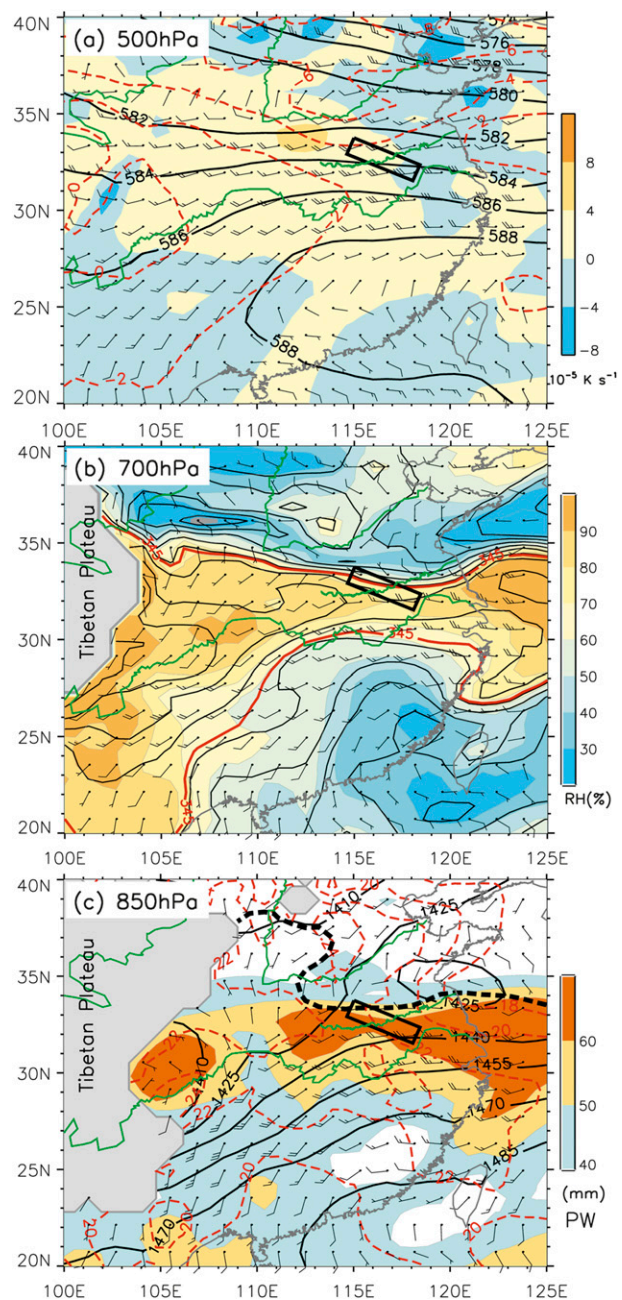


FIG. 4. The ERA-Interim analysis at 0200 BST 8 Jul 2007 of (a) geopotential height (solid, 10 gpm; contoured at intervals of 20 gpm), temperature (dashed, contoured at intervals of 2°C), and thermal advection (10^{-5} K s^{-1} , shaded), superimposed with horizontal wind barbs, at 500 hPa. (b) The equivalent potential temperature (θ_e , contoured at intervals of 4 K, with the 345-K contour in red) and relative humidity (%), shaded, superimposed with horizontal wind barbs, at 700 hPa. (c) The geopotential height (solid, contoured at intervals of 15 gpm), temperature (dashed, contoured at intervals of 2°C), and precipitable water (mm, shaded), superimposed with horizontal wind barbs, at 850 hPa. A full barb is 5 m s^{-1} . The control region is highlighted with a black rectangle in each panel. The gray-shaded regions denote the portions of isobaric surfaces underneath the ground. The thick dashed line in (c) represents $\theta_e = 345\text{ K}$. The Yangtze and Huai Rivers, as well as the Yellow River to the north, are shown as green lines.

TABLE 1. Summary of the simulation design.

Domain	D1	D2	D3
Grid points (x, y)	508×462	733×886	1147×553
Areal coverage (km^2)	6410×5070	2950×2440	1273×613
Grid spacing (km)	10	3.33	1.11
σ values	1, 0.993, 0.983, 0.970, 0.954, 0.934, 0.909, 0.880, 0.834, 0.788, 0.743, 0.697, 0.617, 0.544, 0.478, 0.417, 0.363, 0.313, 0.269, 0.228, 0.192, 0.159, 0.130, 0.104, 0.081, 0.061, 0.042, 0.026, 0.012, 0		
Convective scheme	Kain (2004)	Turned off	Turned off
Cloud microphysics scheme		Morrison et al. (2009)	
Longwave radiation scheme		Mlawer et al. (1997)	
Shortwave radiation scheme		Dudhia (1989)	
Planetary boundary layer scheme		Mellor–Yamada–Janjić (Janjić 1990, 2002)	
Land surface scheme		Thermal diffusion (Chen and Dudhia 2001)	

3. Model description and verification

a. Model description

In this study, the multiscale processes leading to the development of the 8 July 2007 extreme rainfall event are explicitly simulated using a one-way triply nested (10/3.33/1.11 km), nonhydrostatic, cloud-resolving version of the Advanced Research core of WRF (WRF-ARW, version 3.0.1; Skamarock et al. 2008). All the domains are initialized at 1400 BST (i.e., 0600 UTC) 7 July, and then integrated for 24 h. The European Centre for Medium-Range Weather Forecasts (ECMWF) Interim Re-Analysis dataset (ERA-Interim; Dee et al. 2011, available online at <http://www.ecmwf.int/research/era/do/get/era-interim>) is used for the model initial conditions and the outermost lateral boundary conditions updated every 6 h. The configuration of the grids and the model physics parameterizations are summarized in Table 1. Figure 1a shows the three domains used, while Fig. 1b shows better the topographical features of interest. The control box is located about 100 km downstream of Mount Dabie in central China. However, a sensitivity experiment with the Dabie topography removed produces negligible changes in the simulated convective evolution and surface rainfall distribution (not shown). In the next three subsections, we verify the 24-h simulation of the extreme rainfall event against the 8-km-resolution rain-gauge-based hourly rainfall analysis, the mosaic radar reflectivity data, and the mesoscale meteorological features observed at the surface stations.

b. Surface rainfall verification

Figure 2 compares the 14-h accumulated rainfall between the model-simulated and observed results. Note that the control boxes in all figures showing the simulated results have been shifted 40 km to the northeast of the one used in the observed due to the presence of location and timing errors in the simulated rainfall; these

errors could be attributed to the use of the large-scale initial conditions with little mesoscale information and uncertainties in association with the model physical schemes. With these limitations in mind, we may state that the model reproduces reasonably well the general orientation and elongated rainfall distribution as observed, especially the extreme rainfall in the middle portion of the rainfall belt. In particular, the model produces a peak rainfall amount of 234 mm compared to the observed amount of 298 mm. This 64-mm rainfall difference is about half of that in the cloud-resolving study of another YHRB torrential-rainfall event examined by ZZ12. However, the model underproduces the rainfall amount to the northwest of Wangjiaba; otherwise, it would reproduce the west–east-oriented extreme rainfall belt as observed (cf. Figs. 2a and 2b).

Figure 5 compares the time series of the control-box-averaged hourly rainfall rates between the observed and simulated results, after grouping the 8-km resolution observed and the model-simulated hourly rainfall rates into three ranges: heavy, medium, and light, which are defined as the rates of greater than 15, between 5 and 15, and between 0.1 and 5 mm h^{-1} , respectively. Note that the rainfall rates are calculated for the observations and the numerical simulation using their respective control boxes, which are different from each other (Fig. 2). The observed total rainfall rates, dominated by the heavy rainfall rates, revealed three stages of the storm development: (i) a growing stage from 0000 to 0730 BST 8 July, during which period the hourly rainfall rate increased continuously, especially between 0330 and 0730 BST 8 July; (ii) a steady-state stage, in which the hourly rainfall kept nearly constant during a period of about 5 h; and (iii) a weakening stage when the rainfall rate exhibited marked decreases after 1200 BST 8 July (Fig. 5a).

The model captures well the total, heavy, medium, and light rainfall rates during the growing stage. The

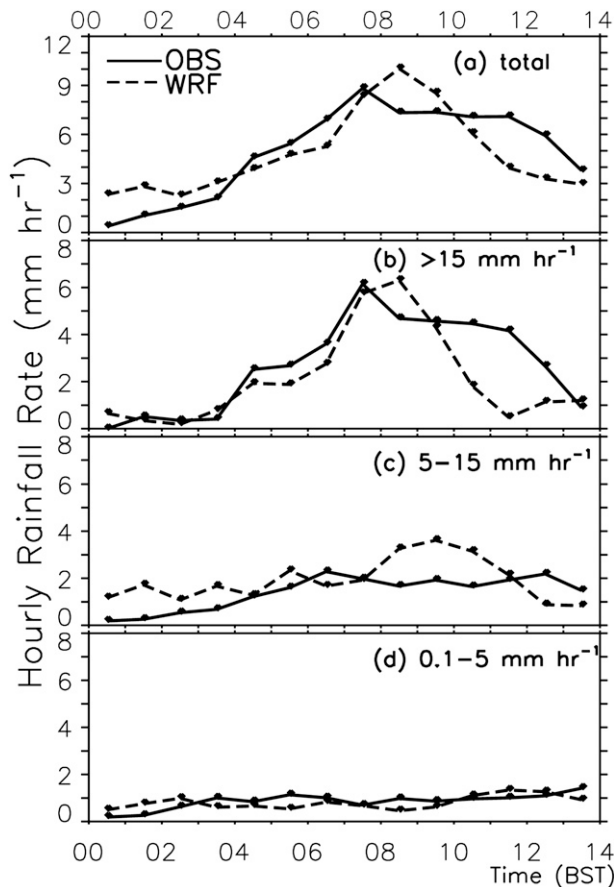


FIG. 5. Comparison of the time series of the hourly rainfall rates (mm h^{-1}), averaged over the control region, during the period 0000–1400 BST 8 Jul 2007 between the observations (solid) and the D3 simulation (dashed) for (a) the total and (b) heavy ($>15 \text{ mm h}^{-1}$), (c) moderate ($5\text{--}15 \text{ mm h}^{-1}$), and (d) light ($0.1\text{--}5 \text{ mm h}^{-1}$) rainfall rates. The rainfall rates at individual grid points are summed up for each rainfall category and then divided by the total number of grid points over the control region.

peak total and heavy rainfall intensities occur at 0830 BST 8 July—only 1 h later than the observed. The model also appears to reproduce well the total rainfall amount over the control region if the hourly total rainfall rates, given in Fig. 5a, are integrated for the 14-h study period. However, the model appears to fail in reproducing the steady rainfall stage, as the simulated total rainfall decreases too rapidly after 0830 BST 8 July. This is mainly associated with the simulated heavy rainfall portion (cf. Figs. 5a and 5d), suggesting that the simulated MCS under study weakens too rapidly. On the other hand, the model overproduces rainfall at the medium intensity during most of the maintenance stage, which could account partly for the too rapid decrease in the heavy rainfall amount (cf. Figs. 5c and 5d). Note that both the observed and simulated light rainfall, including the total amount and coverage, account for less than 5% of the

total rainfall, which is consistent with a small coverage area of stratiform rainfall associated with the MCS (cf. Figs. 5b and 3), as compared to some other linear MCSs shown by Houze et al. (1989), Zhang and Gao (1989), and Parker and Johnson (2004).

c. Radar reflectivity verification

Figure 6 shows the maps of the simulated radar reflectivity, calculated following Smith (1984) and Luo et al. (2010), which should be compared to those shown in Fig. 3. Due to the delayed precipitation spinup, the first simulated reflectivity map is shown 3.5 h later than the observed (i.e., at 0330 BST 8 July). The model produces an MCS to the southwest of Wangjiaba, whose patterns of behavior are similar to those of WH (cf. Figs. 6a–d and 3a–d), but it lags 2–3 h behind the observed and has a larger area of coverage. In spite of these shortcomings, the model reproduces the backbuilding and subsequent organization of convective cells into the west–east-oriented rainbands over the western portion of the control region, especially during the 3-h growing stage of 0330–0630 BST 8 July (Figs. 6a–d). Like those shown in Fig. 3, these rainbands become southwest–northeast oriented and propagate southeastward after moving to the east of the Huai River.

Although it is not possible to compare the convective cells one by one between the observation and simulation, it is encouraging that the model reproduces the continuous initiation of convective cells over an elongated region, as highlighted by box A in Figs. 6a–d, to the northwest of Wangjiaba. Moreover, the model reproduces five or six rainbands at the mature stage (Figs. 6e–g), with both the width and the length scales close to those observed. Because the model fails to reproduce another (weak) rainband 6 between the mei-yu front and the quasi-linear MCS (cf. Figs. 6e–g and 3e–g), it produces a contiguous region of high reflectivity resulting from the echo training and subsequent weakening of convective cells along individual rainbands. This appears to be responsible for the overproduction of rainfall with medium rates shown in Fig. 5c. The simulated MCS shows signs of dissipation after 1100 BST 8 July, which is 1 h earlier than the observed, as is also indicated by Fig. 5a.

d. Mesoscale surface verification

Figure 7 compares the simulated mesoscale surface features shortly after the initiation (i.e., 0200 BST) and near the end of the mature stage (i.e., 1200 BST) of the MCS of interest to those from the observations. Figures 7a and 7b are used herein to indicate how well the model reproduces a west–east-elongated rainfall band from previous convective activity that occurred in the late

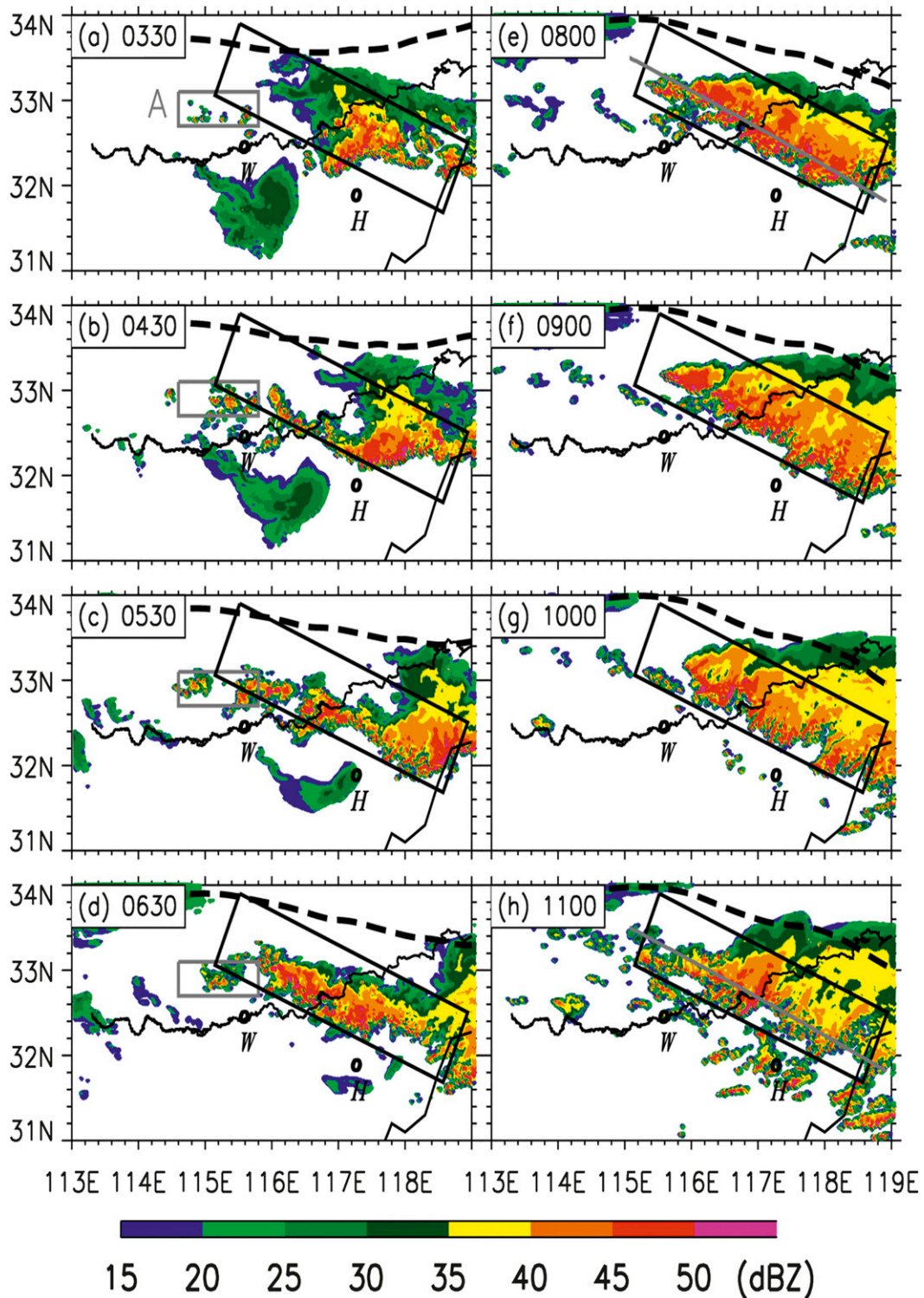


FIG. 6. (a)–(h) As in Fig. 3, but for the D3 simulation at the following selected times: 0330, 0430, 0530, 0630, 0800, 0900, 1000, and 1100 BST 8 Jul 2007. (a)–(d) The gray rectangle represents the region where the continuous CIN occurs during the early development stage of the linear MCS, referred to as region A in the text. (e), (h) The gray lines represent the locations of cross sections used in Figs. 12a and 12b, respectively.

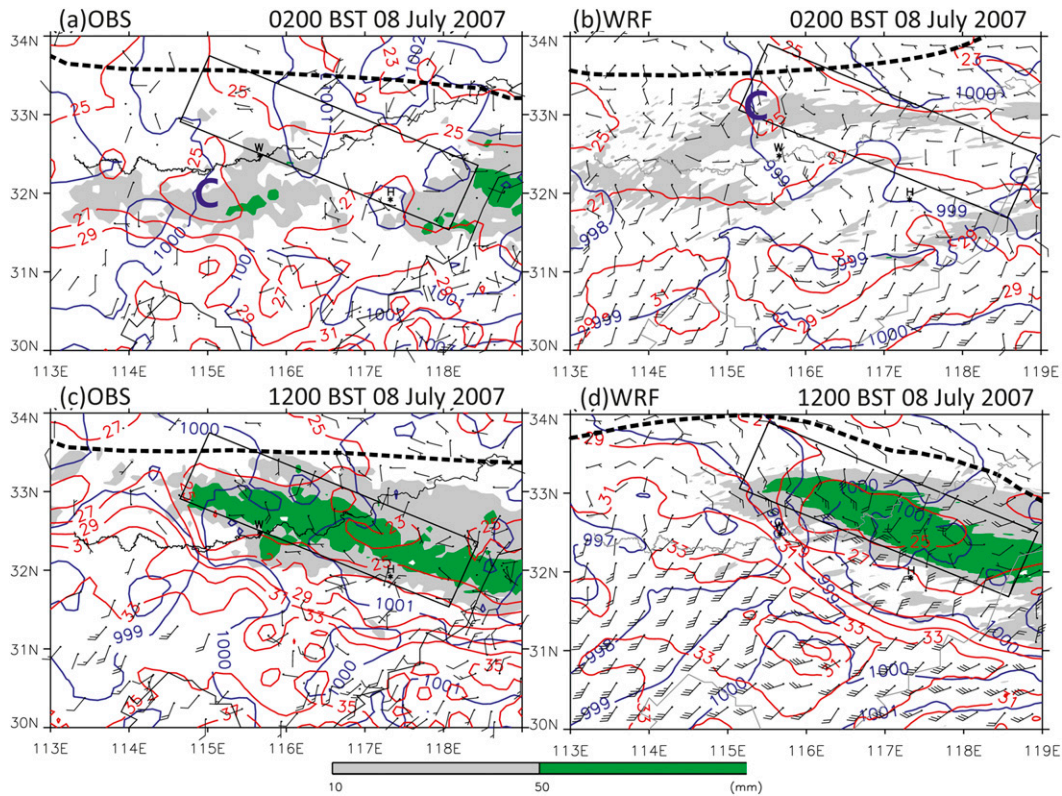


FIG. 7. Comparison of the surface temperature (contoured in red at 2°C intervals) and sea level pressure (contoured in blue at 1-hPa intervals), superimposed with horizontal wind barbs from (a),(c) observations collected at the surface meteorological stations and (b),(d) the simulation valid at (a),(b) 0200 and (c),(d) 1200 BST 8 Jul 2007. Note that a full barb is 2.5 m s^{-1} . Shading denotes 12-h accumulated rainfall amounts (mm). Letter C denotes the local minimum temperature. The black rectangle in each panel denotes the control region.

afternoon and evening hours of 7 July. The convective activity left behind a cold dome with a minimum surface temperature of 25°C to the south of the western control region, as compared to that of 29°C in the rainfall-free regions (Fig. 7a). The model reproduces the development of the convective activity and the cold dome (Fig. 7b), but with the cold center being located close to 100 km to the northeast of the observed (cf. Figs. 7a and 7b). As will be shown in section 4, the cold dome plays a critical role in the initiation of the quasi-linear MCS at midnight.

The convectively generated surface features at the mature stage show more clearly perturbations of surface temperature, horizontal winds, and surface pressure after the quasi-linear MCS had lasted for about 5 h (cf. Figs. 7c and 3t–x). One can see the development of an elongated cold pool corresponding to the quasi-linear MCS and the formation of a pressure ridge in the vicinity of the control region. The cold dome had a minimum surface temperature of 23°C, while surface temperatures in the rain-free area to the south were 33°C and warmer. Such a large thermal gradient (i.e., 10°C in 120 km) generated cold outflows converging

with the southwesterly flows that were about 100 km to the southwest of the MCS. In spite of the intense cold outflow, deep convection occurred only over the control region. The model reproduces, at least qualitatively, the convectively generated cold pool, a meso- β -scale pressure ridge, cold outflows converging with the southwesterly flows, and large thermal contrasts along the leading edge of the outflows during the mature stage (cf. Figs. 7d and 7c). The simulated surface winds are slightly larger than those observed owing to the interpolation of their model surface values to 10 m AGL.

Given the general agreement between the simulation and observations in the surface rainfall distribution, mesoscale surface features, and the development of the quasi-linear MCS, we may use the convection-permitting simulation along with more detailed observational analyses to address the questions raised in section 2.

4. Convective initiation

In this section, we wish to use the model simulation and observations to understand why convective initiation

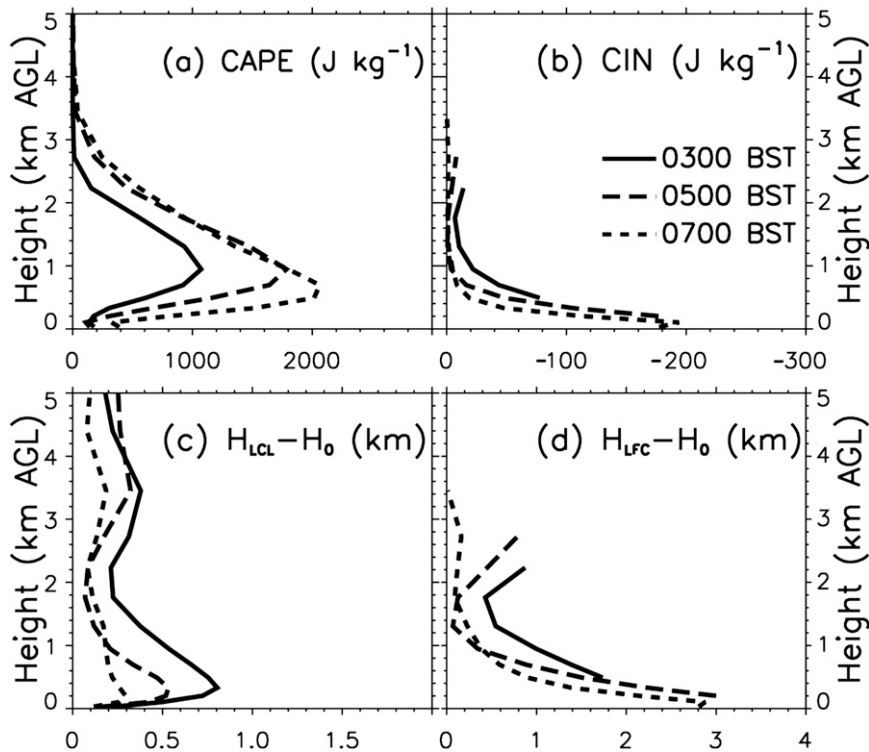


FIG. 8. Vertical profiles of environmental (a) CAPE (J kg^{-1}) and (b) CIN (J kg^{-1}) derived from parcel ascents from various vertical levels averaged over region A (shown in Figs. 6a–d) in D3 at 0300, 0500, and 0700 BST 8 Jul 2007. The corresponding profiles of the distance (km) from the parcel’s lifting level to its (c) LCL and (d) LFC.

could continuously occur in the western portion of the control region during the early development of the linear MCS. Major factors that are relevant to convective initiation at night include convective available potential energy (CAPE), convective inhibition (CIN), and the level of free convection (LFC) and lifting condensation level (LCL) that are derived from parcel ascents at different vertical levels. Here, they are calculated using the D3 simulation over a rectangular area of $120 \text{ km} \times 40 \text{ km}$ near the western edge of the control region (i.e., region A in Figs. 6a–d).

Figure 8 shows vertical profiles of the region-A-averaged values of the above-mentioned parameters at 0300, 0500, and 0700 BST 8 July 2007. Of importance is that CAPE (CIN) increases (decreases) from 0100 to 0700 BST below 3 km AGL, except near the surface where both CAPE and CIN remain nearly unchanged at about 200 and -200 J kg^{-1} , respectively. The relatively small CAPE and large (negative) CIN values near the surface are consistent with the simulated cold dome produced by a previously dissipated MCS (Fig. 7b). Note an elevated layer of the maximum CAPE that is centered at about 1 km AGL with its magnitude increasing from 300 J kg^{-1} at 0100 BST to 1000 J kg^{-1} at 0300 BST

and then to 2000 J kg^{-1} at 0700 BST. CIN nearly vanishes during the period 0400–0700 BST 8 July immediately above the level of the maximum CAPE (i.e., about 1 km), where the corresponding LCL and LFC are only 100–200 m above the parcel’s originating level. These results suggest that the atmospheric conditions over the western portion of the control region are favorable for convective initiations with some small lifting needed, especially for air parcels originating from 1 to 2 km AGL. Moreover, the increasing CAPE and decreasing CIN coincide well with the continuous initiations of convective cells in the western portion of the linear MCS during the period of 0300–0800 BST 8 July (cf. Figs. 8a,b and 6a–d).

One may ask: Where is the source of the unstable air causing the increasing CAPE? What mechanism is responsible for the initiation of convective cells? To answer these questions, backward trajectories are calculated for the period of 0600–0000 BST 8 July 2007 using the D3 simulation outputs at 1-min intervals, following the technique of McGregor (1993) and Zheng et al. (2013) with third-order precision. A total of 150 grid points at 1 km AGL in region A, where the peak CAPE and minimum CIN are on average located, is

selected. As shown in Fig. 9a, most air parcels could be traced 6 h backward to 280–300 km to the southwest of region A, where higher- θ_e air is present (e.g., 364 compared to 348 K in region A).

Figure 9b shows the time evolution of the mid-80th percentile of trajectories (i.e., between the 15th and 135th trajectories) that arrives at certain vertical levels but at any point in the (x, y) plane, because the top and bottom 10th percentile of the trajectories are considered to be outliers and should be excluded in the trajectory analysis. One can see that most of the air parcels traced in the southwesterly flows remain at about 600 m AGL with little vertical displacement until 0250 BST 8 July when they begin to ascend up to 1 km AGL (cf. Figs. 9b and 8a,b). Since there is little diabatic heating involved, this ascent must follow isentropic surfaces above the cold dome from the previous convective activity (e.g., associated with WH; Figs. 6a–c), just like those shown by Banacos and Schultz (2005; see their Fig. 2c) and ZZ12. The isentropic ascending motion occurs near the southwestern edge of sharp high- θ_e gradients (i.e., near the southern end of an elongated box indicated by dashed lines in Fig. 9a). A vertical cross section of the zonally averaged θ_e and moisture fluxes with a width of 40 km, taken from the location of the sharp high- θ_e gradients northeastward, is given in Fig. 9c, showing that a higher- θ_e air tongue as large as 364 K, with a large moisture flux tongue above, ascends over an underlying cold dome northeastward into the western portion of the control region. It is this overrunning higher- θ_e tongue that is responsible for increasing the CAPE at 1 km AGL (Fig. 8a), leading to the continued conditional instability in region A (Figs. 6a–d).

In summary, both the larger-scale monsoonal flow and the mesoscale surface cold dome left behind by the previous convective activity play important roles in controlling the timing and location of convective initiation. While the importance of high- θ_e monsoonal flow in generating heavy mei-yu rainfall is well recognized (e.g., Chen et al. 2010), little evidence has been shown previously on the close linkage between the convective activity occurring during the previous afternoon-to-evening hours and the subsequent nocturnal convective development along a mei-yu front. The above result suggests the possible relationship between the two observed rainfall peaks in the diurnal variation of the mei-yu rainfall over YHRB.

5. Echo- and band-training processes

Previous studies have shown that linear MCSs tend to favor the generation of extreme rainfall through the echo-training process (Houze et al. 1990; Doswell et al.

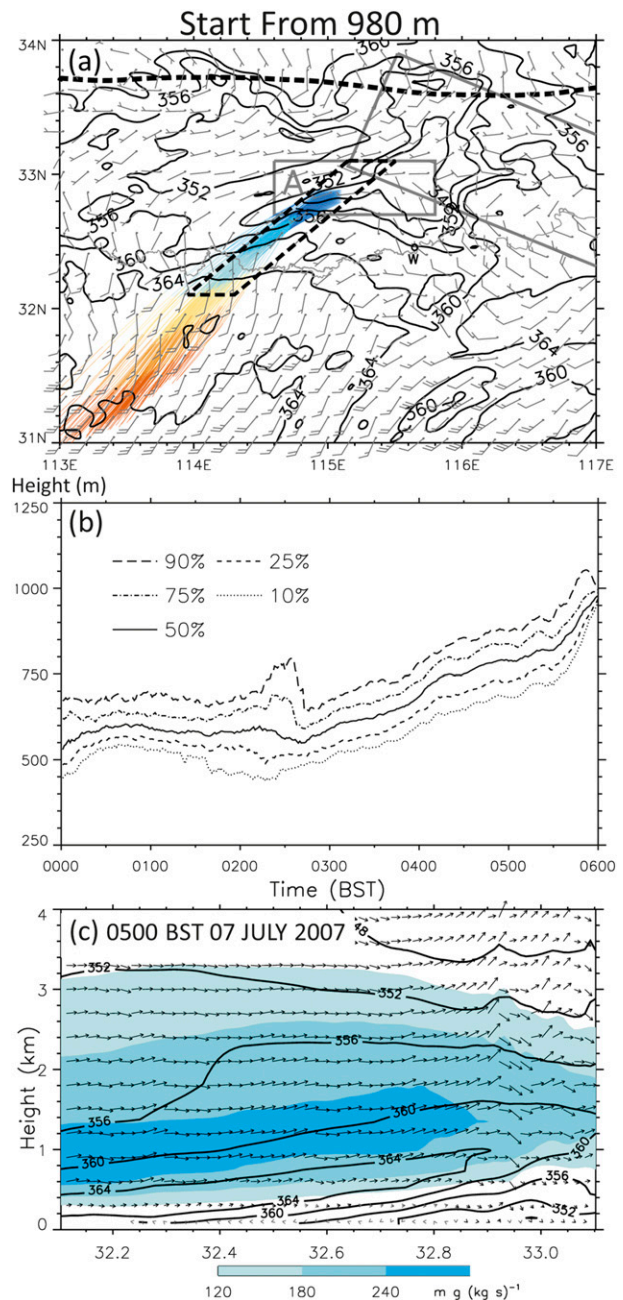


FIG. 9. (a) Horizontal projection of the 150 backward trajectories started from 980 m AGL (colors from blue to orange denote the times from 0600 BST backward to 0000 BST 8 Jul), overlaid by wind barbs at 980 m AGL (a full barb is 5 m s^{-1}) and θ_e at 4-K intervals at 240 m AGL at 0300 BST 8 Jul 2007 (see text for details). A rectangular box (A) is used to indicate the region of convective initiation (also see Figs. 6a–d). (b) The time–height cross section of the mid-80th percentile of the trajectories. (c) Vertical cross section of θ_e (contoured at 4-K intervals), in-plane flow vectors, and the moisture flux [shadings, m g (kg s)^{-1}], $|\mathbf{V}|q_v$, where \mathbf{V} is the horizontal wind vector and q_v is the mixing ratio of the water vapor, at 0500 UTC 8 Jul 2007 along the southwest–northeast-oriented narrow zone as dashed in (a).

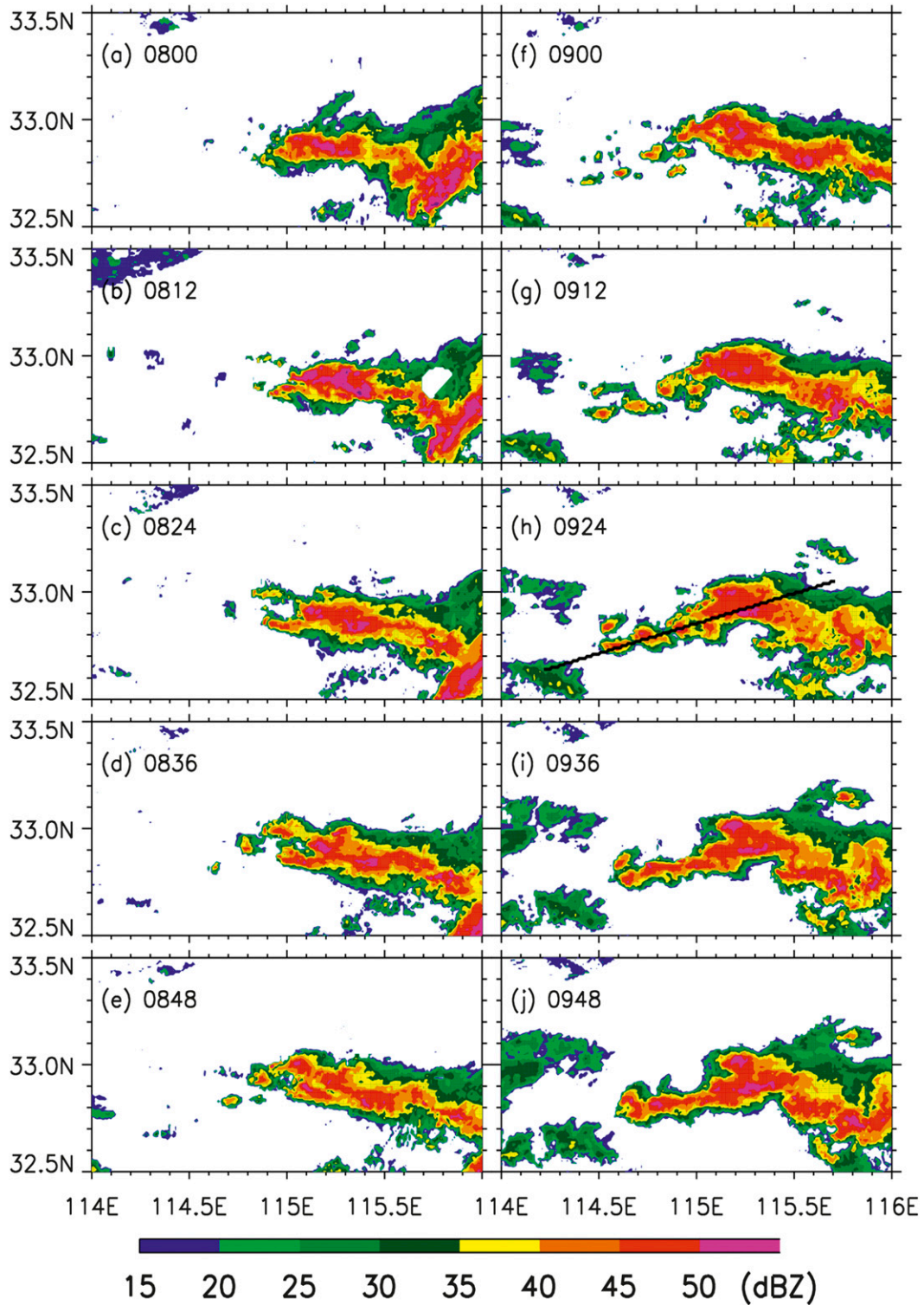


FIG. 10. (a)–(j) Radar reflectivity (dBZ) at 3-km AGL derived from the mosaic reflectivity data at intervals of 12 min during 0800–0948 BST 8 Jul 2007. The black line in (h) represents the location of the cross section used in Fig. 12a.

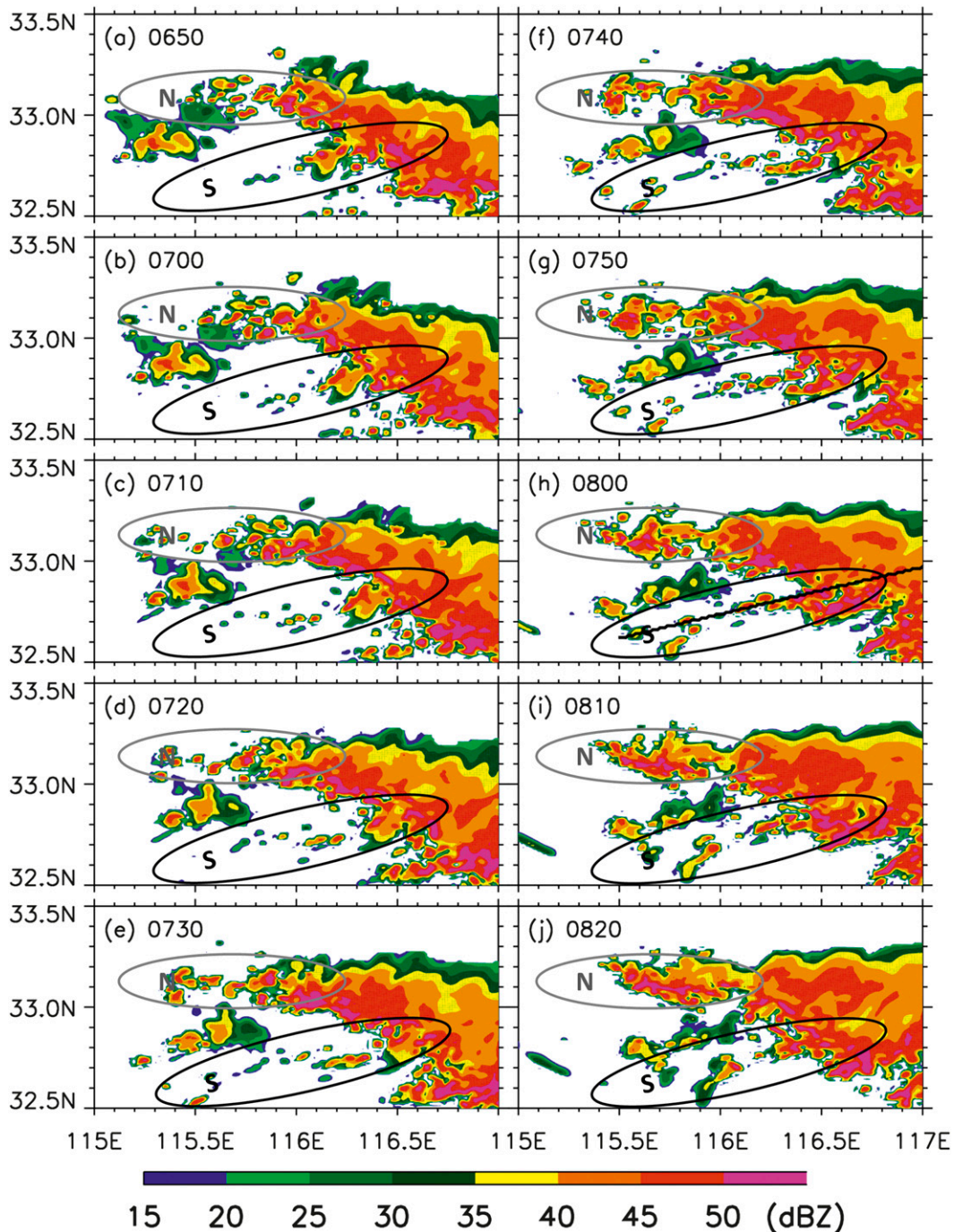


FIG. 11. As in Fig. 10, but for the simulated radar reflectivity at intervals of 10 min from D3 during 0650–0820 BST 8 Jul 2007. Ellipses (N and S) denote the regions of convective backbuilding. The black line in (h) represents the location of the cross section used in Fig. 12b.

1996; Schumacher and Johnson 2005). However, few studies have examined the detailed three-dimensional structures of the linear MCSs due to the lack of high-resolution data. As an example, we illustrate the backbuilding process by showing in Fig. 10 the observed

evolution of rainband 10 within a 108-min time window at 12-min intervals. During 0800–0848 BST 8 July, new convective cells were seen being continuously initiated at the western edge of the west–east-oriented rainband moving eastward, leading to its growth from about 60 km

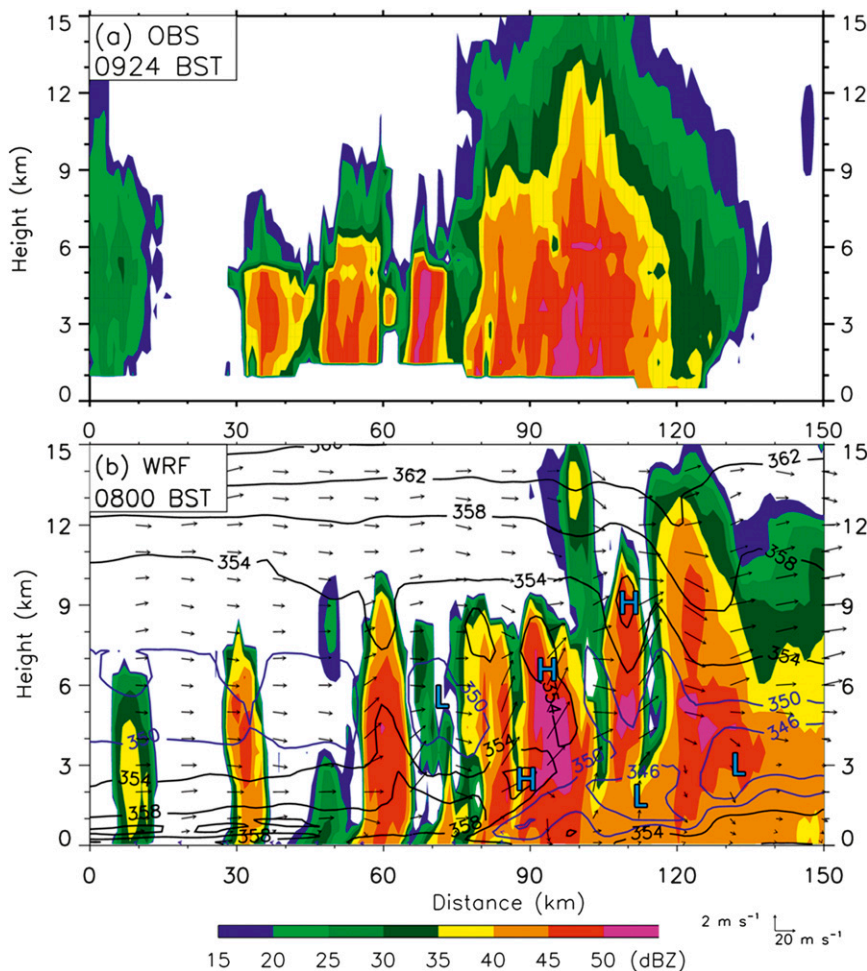


FIG. 12. Vertical cross section of radar reflectivity (dBZ; shadings) from (a) the mosaic radar reflectivity data along a rainband (see Fig. 10h) at 0924 BST and (b) the model-simulated radar reflectivity along a rainband (see Fig. 11h) at 0800 BST 8 Jul 2007. Note that (i) the observed radar reflectivity in the lowest layers was missing as part of the limitations of the radar scan and (ii) the model-simulated θ_e at 4-K intervals and in-plane flow vectors are plotted in (b), but they were not available from the observations. The vertical velocity is multiplied by a factor of 10. Letters H and L denote the local maximum and minimum of θ_e , respectively.

to longer than 100 km in length (Figs. 10a–e). Of interest is that the rainband exhibited little westward propagation until after 0848 BST, when new convective cells began to form continuously and grow in size near its southwestern end. As a result, this rainband extended south-southwestward (Figs. 10e–h). Such a backbuilding phenomenon also appeared in the formation or the growth of the other rainbands (Fig. 3).

Figure 11 shows that although the model could not reproduce the westward building of convective cells as pronounced as the observed along two rainbands (labeled as N and S), it does reveal that the continued convective initiation and growth at their western ends in a quasi-stationary manner. This difference in convective backbuilding could be attributed to either the

distribution of CIN on the west that is larger or the outflow lifting that is weaker than the observed. On the other hand, individual convective cells along the two rainbands keep propagating northeastward, as will be shown in the next section. All of this suggests that the backbuilding process in the simulation is operative, but much slower than the observed.

Figure 12 shows the vertical cross sections of the observed radar reflectivity (Fig. 12a) and the model-simulated radar reflectivity, θ_e , and in-plane flow vectors (Fig. 12b), along a typical near-west–east-oriented rainband in the vicinity of Wangjiaba during the mature stage (see Figs. 10h and Figs. 11h). Both the observations and the simulation show that the individual rainbands consist of discrete, vertically erected convective

cells with increasing reflectivity (i.e., from 35 to 55 dBZ) and cloud-top height rearward, followed by a narrow stratiform region with reflectivity of less than 35 dBZ, indicating the development of convective cells at the different stages of their life cycles. Again, new convective cells are seen being triggered at the western end of the rainband. The simulation provides more detailed information about the dynamical and thermodynamical structures associated with the echo-training process (Fig. 12b). Superimposed on the convective updrafts and downdrafts are along-band flows of $15\text{--}20\text{ m s}^{-1}$ throughout the troposphere before reaching the intense cells where the southwesterly flows in the lowest 4-km layer ascend rearward, just like the front-to-rear ascending flow in the conceptual model of Houze et al. (1989). Obviously, the along-band flows account for the rearward advection of cloud hydrometeors or convective cells and the formation of the stratiform region, which is consistent with the echo-training conceptual model of Doswell et al. (1996). With all the results shown in Figs. 2, 3, 6, 10, and 11, we may state that the continuous convective initiation in region A and the subsequent echo training along the west–east-oriented rainbands are mostly responsible for the generation of extreme rainfall in the present case.

The observed rainband training can also be seen in Fig. 13a, which shows a Hovmöller diagram of the near-west–east-averaged radar reflectivity at 6-min intervals along the ridge axis of the total accumulated rainfall, as given in Fig. 2a. Only the reflectivity data along the central 40-km portion of torrential rainfall (Fig. 2a; i.e., roughly with a total accumulated rainfall amount of 100 mm and greater) are processed. The extreme rainfall region encountered the passage of five major rainbands; they propagate rightward at roughly the same speed of $12\text{--}15\text{ m s}^{-1}$. The band training along the northwest–southeast-oriented quasi-linear MCS appears to favor the maintenance of the rainbands as they could access higher CAPE in the larger-scale west-to-southwesterly flows.

The model also reproduces reasonably well the observed band-training process. One can see that the general rainband structures in Fig. 13b are very similar to those in Fig. 13a, except for some differences in intensity and the timing and location of convective initiations in the western portion of the linear MCS. Of importance is that the model reproduces four or five well-defined rainbands moving along the quasi-linear MCS at the same speed of $12\text{--}15\text{ m s}^{-1}$ as that seen from the radar observations. The model also appears to reproduce reasonably well the temporal and spatial intervals between individual rainbands as well as the westward building of deep convection in the Hovmöller

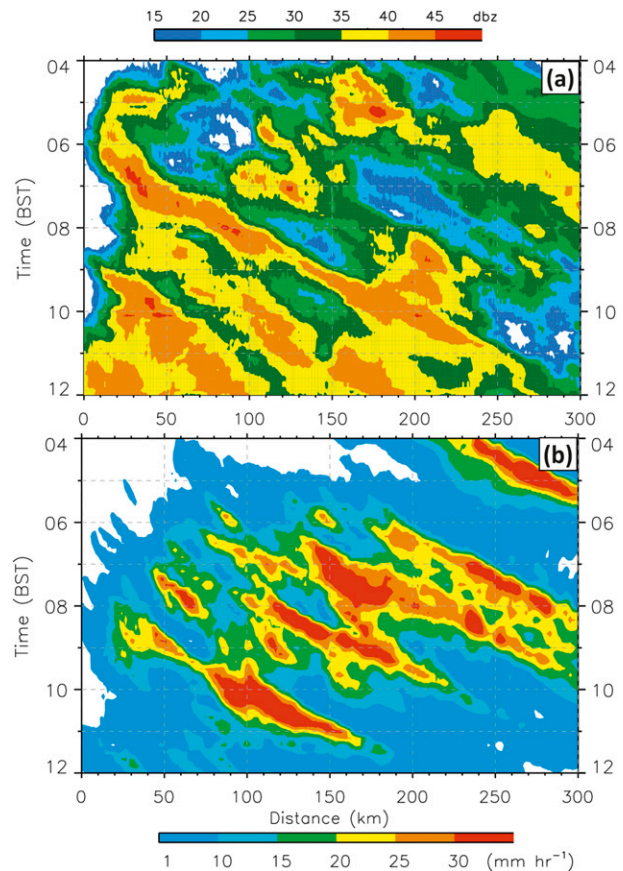


FIG. 13. (a) Time–distance (i.e., Hovmöller) diagram of the observed 6-min radar reflectivities (dBZ) that are west–east averaged along the central portion of the observed rainfall belt (i.e., a narrow zone denoted by dashed lines in Fig. 2a). (b) As in (a), but for the simulated 5-min rainfall rates (mm h^{-1}) that are west–east averaged along the central portion of the simulated rainfall belt (i.e., a narrow zone denoted by dashed lines in Fig. 2b).

diagram. The previously mentioned underestimation of rainfall over the western end of the control box in the simulation (cf. Figs. 2b and 2a) can also be seen by comparing Figs. 13b and 13a.

Vertical cross sections along the leading portion of the quasi-linear MCS in the simulation, given in Fig. 14 show the training scenarios that are similar to those along a rainband. That is, during the mature stage (Fig. 14a), the linear MCS is composed of numerous discrete rainbands with high reflectivity (greater than 50 dBZ) and high cloud depths in the western half of the control region, except for the backbuilding region, and relatively lower ones in the eastern half. The cloud depth appears to be closely related to the magnitude of the incoming elevated environmental- θ_e air that decreases rightward, indicating the decreasing conditional instability rightward. Like the echo training, along-line flows of

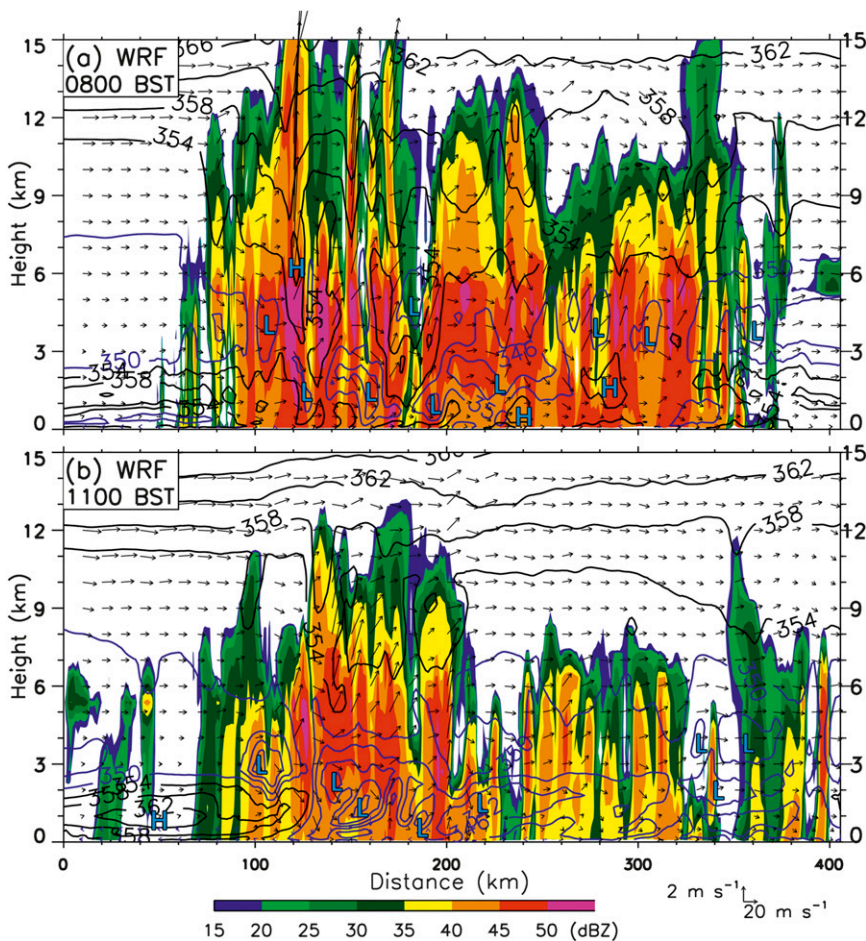


FIG. 14. As in Fig. 12b, but through the leading convective line of the MCS (i.e., gray lines in Figs. 6e and 6h) at (a) 0800 and (b) 1100 BST 8 Jul 2007.

10–20 m s⁻¹ above 5 km AGL and of less than 5–8 m s⁻¹ in the lowest 3-km layer could account for the rightward advection of the rainbands, thus being referred to herein as the rainband training. Clearly, as individual rainbands propagate rightward, new convective cells tend to be initiated at the southwestern end (Figs. 12a and 12b), while old convective cells move rearward along the bands and eventually dissipate in the stratiform region (Fig. 12b). Therefore, the two organizational modes are similar within the context of the training of convective elements, but they differ in their spatial scales and movement directions.

The vertical structures of the quasi-linear MCS during its weakening stage (Fig. 14b) are characterized by decreasing θ_e values in the elevated θ_e layer, except at the northwestern backbuilding segment; decreasing intensity in radar reflectivity, especially in the southeastern segment; and diminishing cloud-top heights along the leading portion of the MCS. These are all consistent with the reduced southwesterly moisture fluxes toward and

the reduced conditional instability over the control region (not shown).

6. Summary and conclusions

In this study, the initiation and organization of a quasi-linear, extreme-rain-producing MCS, occurring along a mei-yu front in eastern China during the midnight-to-morning hours of 8 July 2007, are examined using high-resolution observations of surface parameters and radar reflectivity, as well as a 24-h convection-permitting simulation of the case with the nested-grid spacing of 1.11 km. Large-scale analysis shows that the storm environment was characterized by high precipitable water exceeding 60 mm being transported by moist southwesterly monsoonal flows.

Observational analysis shows that the MCS under study began from the initiation of a few scattered convective storms around the western control region, where high- θ_e air continuously fed by the southwesterly current

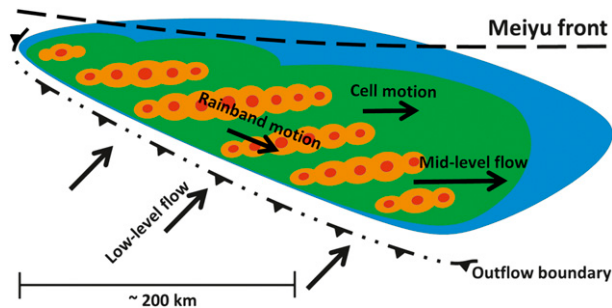


FIG. 15. Schematic diagram of the backbuilding, echo training, and rainband training associated with the quasi-linear-shaped, extreme-rain-producing MCS. Shadings in orange, green, and blue represent radar reflectivity values of roughly 50, 35, and 20 dBZ, respectively. See the text for more details.

isentropically ascended a cold dome left behind by convective activity that occurred during the previous afternoon-to-evening hours. The continuous convective initiation, their organizations into more than eight well-defined west–east-oriented rainbands in the western half of the control region, and the subsequent southeastward propagation of the rainbands led to the formation of the quasi-linear MCS. Although some rainbands were reorganized during their southeastward propagations, their identities could be readily traced. The MCS lasted for 14 h from the appearance of its first rainband to its dissipation, while the life span of individual rainbands ranged from 4 to more than 10 h.

It is shown that although there are some notable differences between the convection-permitting simulation and the observations, the model reproduces reasonably well the above-mentioned meso- β -scale features, including the previously dissipated MCS and the associated cold pool, the orientation and distribution of the quasi-linear MCS, as well as the associated rainfall magnitudes. The model produces a peak rainfall amount of 234 mm compared to an observed amount of 298 mm, both occurring during the middle portion of the linear MCS.

Based on the observational analysis and numerical simulation results, Fig. 15 summarizes the two scales of convective organization taking place during the mature stage of the quasi-linear MCS: one is the eastward echo training of convective cells along individual rainbands and the other is the southeastward band training of the rainbands along the MCS. The echo training appears to be responsible for generating most of the extreme rainfall (to the west of the Huai River), while the band training accounts for the longevity of some rainbands and the formation of the linear MCS. The two organizational modes are similar within the context of “training” of convective elements, but they differ in their

spatial scales and directions of movement. New convection initiates at the western (or southwestern) end of individual rainbands, as the high- θ_e air continuously fed by the southwesterly current ascends the convectively generated cold outflows.

The above conceptual model appears to be similar to that of the extreme rainfall climatology in North America by Schumacher and Johnson (2005) in terms of echo training, but differs in the formation of several parallel rainbands, their subsequent band training along the same path, and the development of little stratiform rainfall. The present quasi-linear MCS also includes a weak rainband, which evolved into a stratiform zone, to the rear of the leading rainbands as a result of the reduced energy supply. Our results also reveal a possible linkage between a mesoscale cold pool, generated by convective activity during the previous afternoon-to-evening hours, and the nocturnal convective initiation leading to the development of an extreme-rain-producing linear MCS with the maximum regional rainfall in the early morning hours. Clearly, more case studies need to be conducted in the future to generalize our findings and gain insights into different convective organizations in the development of extreme rainfall. In a forthcoming study, we will further examine multiscale processes that influencing the formation and evolution of the linear MCS in the present case.

Acknowledgments. We wish to thank the anonymous reviewers for providing constructive comments and suggestions, which significantly helped improve the quality of the manuscript. We would also like to thank Dr. Yongjun Zheng for his assistance in performing the trajectory analysis. This study was jointly funded by the National Basic Research Program of China (973 Program; 2012CB417202), the National Key Technology Research and Development Program of China (2012BAC22B03), the National Natural Science Foundation of China (Projects 41175049 and 41221064), and the Basic Research Funds of the Chinese Academy of Meteorological Sciences (2012Y001). The third author (DLZ) was also supported by NSF Grant ATM0758609 and NOAA Grant NA12NWS4680008. The surface observations and radar data were provided by the National Meteorological Information Center of the Chinese Meteorological Administration, where the WRF simulations were performed.

REFERENCES

- Banacos, P. C., and D. M. Schultz, 2005: The use of moisture flux convergence in forecasting convective initiation: Historical and operational perspectives. *Wea. Forecasting*, **20**, 351–366.

- Chen, F., and J. Dudhia, 2001: Coupling an advanced land surface–hydrology model with the Penn State–NCAR MM5 modeling system. Part I: Model implementation and sensitivity. *Mon. Wea. Rev.*, **129**, 569–585.
- Chen, G. T. J., and C. C. Yu, 1988: Study of low-level jet and extremely heavy rainfall over northern Taiwan in the mei-yu season. *Mon. Wea. Rev.*, **116**, 884–891.
- Chen, H., R. Yu, J. Li, W. Yuan, and T. Zhou, 2010: Why nocturnal long-duration rainfall presents an eastward-delayed diurnal phase of rainfall down the Yangtze River valley. *J. Climate*, **23**, 905–917.
- Chen, S. J., Y.-H. Kuo, W. Wang, Z. Y. Tao, and B. Cui, 1998: A modeling case study of heavy rainstorms along the mei-yu front. *Mon. Wea. Rev.*, **126**, 2330–2351.
- Dee, D. P., and Coauthors, 2011: The ERA-Interim reanalysis: Configuration and performance of the data assimilation system. *Quart. J. Roy. Meteor. Soc.*, **137**, 553–597.
- Ding, Y. H., 1992: Summer monsoon rainfalls in China. *J. Meteor. Soc. Japan*, **70**, 373–396.
- , and J. C. L. Chan, 2005: The East Asian summer monsoon: An overview. *Meteor. Atmos. Phys.*, **89**, 117–142.
- Doswell, C. A., III, H. E. Brooks, and R. A. Maddox, 1996: Flash flood forecasting: An ingredients-based methodology. *Wea. Forecasting*, **11**, 560–581.
- Dudhia, J., 1989: Numerical study of convection observed during the Winter Monsoon Experiment using a mesoscale two-dimensional model. *J. Atmos. Sci.*, **46**, 3077–3107.
- Houze, R. A., Jr., S. A. Rutledge, M. I. Biggerstaff, and B. F. Smull, 1989: Interpretation of Doppler weather radar displays in midlatitude mesoscale convective systems. *Bull. Amer. Meteor. Soc.*, **70**, 608–619.
- , B. F. Smull, and P. Dodge, 1990: Mesoscale organization of springtime rainstorms in Oklahoma. *Mon. Wea. Rev.*, **118**, 613–654.
- Janjić, Z. I., 1990: The step-mountain coordinate: Physical package. *Mon. Wea. Rev.*, **118**, 1429–1443.
- , 2002: Nonsingular implementation of the Mellor–Yamada level 2.5 scheme in the NCEP Meso Model. NCEP Office Note 437, 61 pp.
- Kain, J. S., 2004: The Kain–Fritsch convective parameterization: An update. *J. Appl. Meteor.*, **43**, 170–181.
- , and Coauthors, 2008: Some practical considerations regarding horizontal resolution in the first generation of operational convection-allowing NWP. *Wea. Forecasting*, **23**, 931–952.
- Lean, H. W., P. A. Clark, M. Dixon, N. M. Roberts, A. Fitch, R. Forbes, and C. Halliwell, 2008: Characteristics of high-resolution versions of the Met Office Unified Model for forecasting convection over the United Kingdom. *Mon. Wea. Rev.*, **136**, 3408–3424.
- Luo, Y., Y. Wang, H. Wang, Y. Zheng, and H. Morrison, 2010: Modeling convective-stratiform precipitation processes on a mei-yu front with the Weather Research and Forecasting model: Comparison with observations and sensitivity to cloud microphysics parameterizations. *J. Geophys. Res.*, **115**, D18117, doi:10.1029/2010JD013873.
- , W. Qian, R. Zhang, and D.-L. Zhang, 2013: Gridded hourly precipitation analysis from high-density rain-gauge network over the Yangtze-Huai Rivers basin during the 2007 mei-yu season and comparison with CMORPH. *J. Hydrometeorol.*, **14**, 1243–1258.
- McGregor, J. L., 1993: Economical determination of departure points for semi-Lagrangian models. *Mon. Wea. Rev.*, **121**, 221–230.
- Mlawer, E. J., S. J. Taubman, P. D. Brown, M. J. Iacono, and S. A. Clough, 1997: Radiative transfer for inhomogeneous atmosphere: RRTM, a validated correlated-k model for the long-wave. *J. Geophys. Res.*, **102** (D14), 16 663–16 682.
- Morrison, H., G. Thompson, and V. Tatarskii, 2009: Impact of cloud microphysics on the development of trailing stratiform precipitation in a simulated squall line: Comparison of one- and two-moment schemes. *Mon. Wea. Rev.*, **137**, 991–1007.
- Parker, M. D., and R. H. Johnson, 2004: Structures and dynamics of quasi-2D mesoscale convective systems. *J. Atmos. Sci.*, **61**, 545–567.
- Qian, J. H., W. K. Tao, and K. M. Lau, 2004: Mechanisms for torrential rain associated with the mei-yu development during SCSMEX 1998. *Mon. Wea. Rev.*, **132**, 3–27.
- Schumacher, R. S., and R. H. Johnson, 2005: Organization and environmental properties of extreme-rain-producing mesoscale convective systems. *Mon. Wea. Rev.*, **133**, 961–976.
- Schwartz, C. S., and Coauthors, 2009: Next-day convection-allowing WRF model guidance: A second look at 2-km versus 4-km grid spacing. *Mon. Wea. Rev.*, **137**, 3351–3372.
- Skamarock, W. C., and Coauthors, 2008: A description of the Advanced Research WRF version 3. NCAR/TN-475+STR, 113 pp.
- Smith, P. L., 1984: Equivalent radar reflectivity factors for snow and ice particles. *J. Climate Appl. Meteor.*, **23**, 1258–1260.
- Yu, R.-C., T. J. Zhou, A. Y. Xiong, Y. J. Zhu, and J. Li, 2007: Diurnal variations of summer precipitation over contiguous China. *Geophys. Res. Lett.*, **34**, L01704, doi:10.1029/2006GL028129.
- Yuan, W.-H., R.-C. Yu, H.-M. Chen, J. Li, and M.-H. Zhang, 2010: Subseasonal characteristics of diurnal variation in summer monsoon rainfall over central eastern China. *J. Climate*, **23**, 6684–6695.
- , —, M. Zhang, W. Lin, H. Chen, and J. Li, 2012: Regimes of diurnal variation of summer rainfall over subtropical East Asia. *J. Climate*, **25**, 3307–3320.
- Zhang, D.-L., and K. Gao, 1989: Numerical simulation of an intense squall line during 10–11 June 1985 PRE-STORM. Part II: Rear inflow, surface pressure perturbations and stratiform precipitation. *Mon. Wea. Rev.*, **117**, 2067–2094.
- , —, and D. B. Parsons, 1989: Numerical simulation of an intense squall line during 10–11 June 1985 PRE-STORM. Part I: Model verification. *Mon. Wea. Rev.*, **117**, 960–994.
- Zhang, M., and D.-L. Zhang, 2012: Subkilometer simulation of a torrential-rain-producing mesoscale convective system in East China. Part I: Model verification and convective organization. *Mon. Wea. Rev.*, **140**, 184–201.
- Zhao, S.-X., L.-S. Zhang, and J.-H. Sun, 2007: Study of heavy rainfall and related mesoscale systems causing severe flood in Huaihe River basin during the summer of 2007 (in Chinese). *Climatic Environ. Res.*, **12**, 713–727.
- Zheng, Y.-J., G.-X. Wu, and Y.-M. Liu, 2013: Dynamical and thermal problems in vortex development and movement. Part I: A PV–Q view. *Acta Meteor. Sin.*, **27**, 1–14.
- Zhou, T.-J., R. Yu, H. Chen, A. Dai, and Y. Pan, 2008: Summer precipitation frequency, intensity, and diurnal cycle over China: A comparison of satellite data with rain gauge observations. *J. Climate*, **21**, 3997–4010.